Valence-electronic effect on low-temperature phase stability of the omega phase

Valence-electronic effect on low-temperature phase stability of the omega phase

Takeshi Yano, Tomoaki Uchida, Yusuke Shimizu and Naohisa Takesue

Department of Applied Physics, Graduate School of Science, Fukuoka University, Nanakuma, Jonan-ku, Fukuoka 814-0180, Japan

E-mail: takesue@cis.fukuoka-u.ac.jp

Abstract
Low-temperature phase stability of the omega phase of BCC binary Ti alloys and Zr alloys has been expected qualitatively by first-principles population analysis of the molecular orbitals. The analysis was performed using the cluster models with 3d or 4d transition elements for binary-alloying. The results show that the positive overlap population in the valence band tends to shift downward along the energy axis as the e/a ratio is increased. This tendency implies no electronic contribution to the stability of the Zr–Ti system, having the minimum ratio, 4. To confirm this expectation, electron diffraction was carried out on single-crystal Zr–50 at.% Ti, and also Ti–24 mass% V used as the reference. The superlattice reflections of the omega phase, given by the BCC reduced wavevector $q = (2/3 + \Delta, 2/3 + \Delta, 2/3 + \Delta)$, were observed at ~100 K and room temperature. The results indicate that temperature dependence of the intensity distribution of the Zr alloy is much less significant than that of the Ti alloy. The x-ray diffraction measurements were also done on single-crystal Zr–30 at.% Ti, –35 at.% Ti, –50 at.% Ti to double check the temperature dependence. The results provide a feature which is quite similar to that obtained by the electron diffraction. All experimental results are found consistent with those of the population analysis.

1. Introduction

BCC zirconium (Zr) alloys and titanium (Ti) alloys usually have a lattice instability, called the Kohn anomaly, which is observed as a distinct dip at reduced wavevector $q = (2/3, 2/3, 2/3)$ in the phonon dispersion curve of the $\langle 111 \rangle$ longitudinal acoustic (LA) mode [1–3]. The instability is a notional freezing of the low-dimensional charge density waves (CDW) [4–6]. The substantial freezing can be realized through relaxation of the lattice distortion which is caused by supersaturated atomic vacancies frozen in by rapid cooling from high temperature, and leads to the formation of the metastable product, called the omega phase. Its crystal structure is given in general by cooperative atomic displacements with incommensurate reduced wavevector $q = (2/3 + \Delta, 2/3 + \Delta, 2/3 + \Delta)$, where Δ is the incommensurability and has a value typically a fraction of 0.1 in reciprocal lattice units (rlu). If $\Delta = 0$, the structure

is commensurate and has hexagonal symmetry [1, 7, 8]. Otherwise, the structure is incommensurate [9–11] and has no six-fold axis but one three-fold instead. A significant difference between the two structures is seen by diffraction experiments [9–11]. Figure 1(a) is a schematic drawing of the diffraction pattern in the $(1\bar{1}0)$ reciprocal lattice plane. The solid circles are locations of the fundamental Bragg reflections, and the open circles the superlattice reflections given by the commensurate structure. The portion of two adjacent reflections $(2/3, 2/3, 2/3)$ and $(4/3, 4/3, 4/3)$ are expanded and given in figure 1(b). Nonzero Δ slightly shifts the superlattice positions along the [111] direction and causes diffuse scattering around the superlattice positions [9–11], which can be explained based on structural models by the short-range spatial correlations, i.e., a sort of stacking fault of the (111) planes depicted by solitons [12], or complex-arrayed imperfections [13–16]. The models are almost complements of the one based upon the CDW which physically explains the lattice modulation.
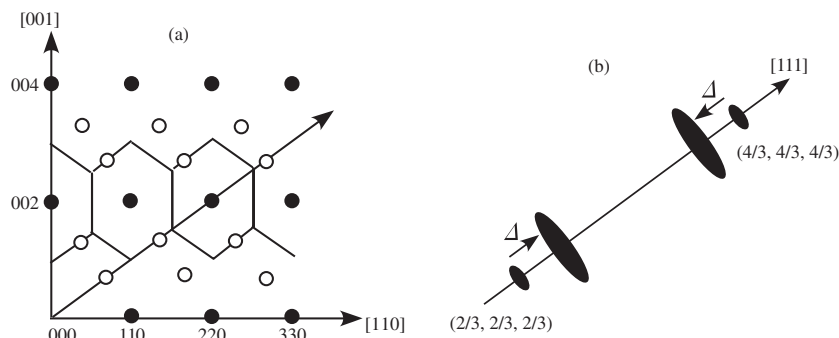
Figure 1. The BCC (1$\bar{1}$0) reciprocal lattice plane. Hexagons in (a) are the Brillouin zone boundaries. Ellipses in (b) schematically show the intensity distribution of the two spots for nonzero Δ.

The electron–lattice coupling nature is readily observed by diffraction experiments as a function of valence-electronic concentration (e/a ratio) [9–11, 17] and temperature [18–20], which is the case with solid solutions containing other transition metals such as vanadium (V), chromium (Cr), iron (Fe), molybdenum (Mo), niobium (Nb), etc; the elements have e/a values higher than those of Ti and Zr whose values are 4. Results of the previous studies indicate that both increasing e/a and elevating temperature commonly have the following three effects [20]: (1) increase of Δ, (2) weakening of the superlattice intensity, and (3) broadening of the intensity distribution. These effects are caused by an excess of the valence electrons or a thermal disturbance of the spatial electronic configurations which prohibits evolution of the long-range stable CDW, and can be thought as a measure of phase stability of the omega phase. The observed temperature dependence of the intensity distribution was qualitatively explained by first-principles molecular-orbital population analysis based on the rigid-band concept [20].

Among the alloy systems, Zr–Ti alloys, which are also known to form the omega phase, are expected to have a quite unique electronic feature since the e/a ratio of this system is 4, independent of the concentration [1, 17, 21]. Therefore, homogeneous distribution of the valence electrons is realized and leads to a phase formation of the uncoupled type which has no way to cause the CDW. In this case, the phase must be formed simply through mechanical relaxation to the distortion originating from the vacancies and additionally an atomic size difference [17] between the two elements, suggesting that temperature dependence of the phase stability is appreciably less significant compared with that of the CDW systems. To verify this expectation, we have performed first-principles calculations using alloyed cluster models of the omega phase and have qualitatively evaluated the phase stability considering the obtained atomic bonding nature, this was followed by electron and x-ray diffraction to confirm the relatively small temperature dependence of the intensity distribution of the superlattice reflections.

2. Cluster calculation

A discrete-variational (DV) Xα cluster method [22] and its computer code SCAT [23] were employed for population
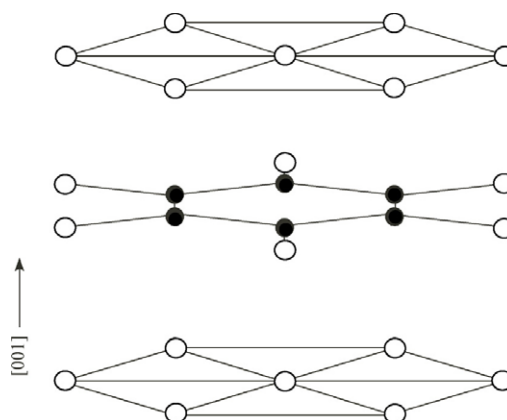
Figure 2. The 26-site cluster model based on space group $P6/mmm$. The model consists of the four (001) planes. The open and solid circles are locations of the solvent and solute atoms, respectively.

analysis of the molecular orbitals (MO). The calculation was performed based upon the density functional theory [22], where the total charge density of the cluster is used as the functional. The MO wavefunctions were given by assuming linear combination of the atomic orbitals (AO) whose fractional coefficients were determined when the self-consistent charge was realized. The obtained eigenfunctions were used to compute AO's density of states (DOS) in each MO and overlap population (OP) between all atomic pairs. The results are presented with respect to the achieved stationary eigenvalues.

Figure 2 illustrates a frame of the cluster model based on the commensurate structure. The frame is constructed by four (001) planes of the hexagonal system, and consists of 26 atomic sites given by special positions of $P6/mmm$. The 20 open and 6 solid circles in the figure indicate locations of the solvent and solute atoms, respectively, providing a solute concentration of 6/26, i.e., ~23 at.%, which is the typical value for phase formation [17]. The calculation was carried out on the Zr and Ti alloys including the solvent end-member systems for the comparison. Alloying elements selected for modeling on the Zr alloys are Ti, Nb, and Mo, and those on the Ti alloys are V, Cr, and Fe. The lattice parameters used are of the typical values, $a = 0.510$ nm and $c = 0.313$ nm for the Zr systems,
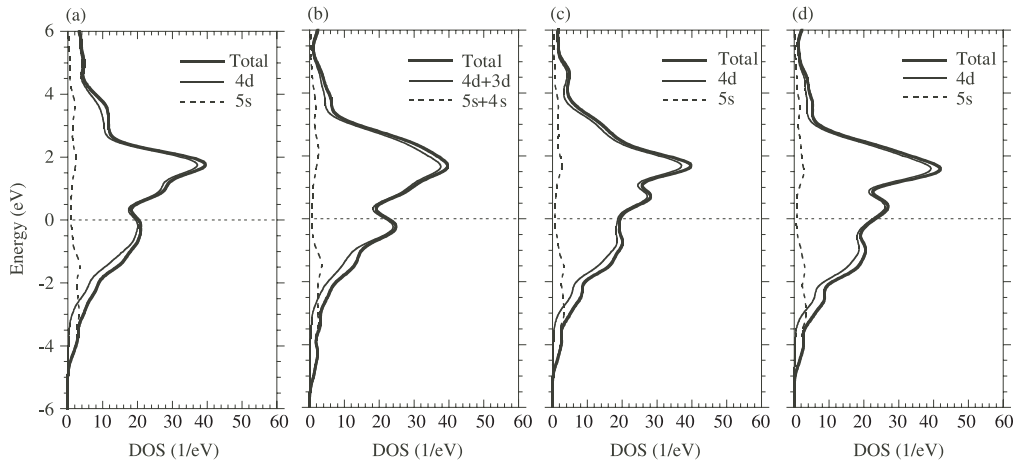
Figure 3. Total and partial DOS curves near the Fermi level for (a) the pure Zr, (b) Zr–Ti, (c) Zr–Nb, and (d) Zr–Mo systems. Each partial DOS for the alloy consists of the components of the two elements.

and $a = 0.470$ nm and $c = 0.288$ nm for the Ti systems [20] (one of the authors, N Takesue, had used the latter two values for Ti–V alloys previously), giving all atomic coordinates of the models in the absolute scale.

3. Experimental details

Single-crystal Zr alloys containing 30, 35, 50 at.% Ti were grown using an infrared zone-melting furnace (FZ-T-4000-H, Crystal Systems). Each of the as-grown specimens was sliced into a few disks with a {110} face whose sizes were typically 6mm in diameter and 1–2 mm in thickness. The samples were annealed at 1373 K for 30 min, and were then quenched in room-temperature water, followed by conventional surface treatment by means of mechanical polishing and chemical etching [20]. The crystal quality was prechecked by x-ray diffraction, giving typical diffraction patterns of single crystals. Some of the prepared disks of each system were supplied for electron diffraction and the others for x-ray diffraction.

The disks for the electron diffraction were further sliced and mechanically polished, giving the foil specimens. The specimen of Ti–24 mass% V was also prepared from the crystal which was employed in the previous x-ray diffraction study done by Takesue [20], and was used to obtain the reference data for comparison with those of the Zr alloys. The foils were thinned down by ion milling (PIPS 691, GATAN), and were provided for the observation. The observation was performed by using an electron microscope (JEM-2100, JEOL), and temperature dependence of the intensity distribution was inspected qualitatively. The intensity distribution in the BCC {110} diffraction pattern was observed at room temperature and at ∼100 K. The intensity data were taken by using imaging plates. The stored data were all digitized using an imaging-plate reader. The concentrations of the samples were determined through EDS analysis by scanning several regions in the foils, which provided the differences from the prepared values, ±0.5 at.%, with no significant segregation.

A laboratory-type single-crystal low-temperature x-ray diffraction system was employed for the experiment. The

instrumental and optical setups on this system are exactly the same as the ones given in [20]. The system was equipped with a Mo rotating anode. The Kα beam was given by a pyrolytic graphite monochromator with the (002) face reflecting, and was collimated using incident and receiving double slits. The measurements were performed at 30 K through 300 K with incrementally changing temperature. At each temperature, the crystal orientation of each sample was determined in terms of the fundamental reflection angles for the Kα_1 line, and the intensity distribution of the superlattice position (4/3, 4/3, 4/3) was then observed quantitatively.

4. Results and discussion

Figures 3(a)–(d) show total and partial DOS curves near the Fermi level for the pure Zr, Zr–Ti, Zr–Nb, and Zr–Mo systems, respectively, where the Fermi level, denoted by E_f in the text, is given by the horizontal lines drawn at an origin of the energy axis. The total DOS in each figure indicates a distinct band near E_f, and the comparison with the partial DOS tells us that main components of the band are the 4d AOs of the 4d transition metals, also including the 3d AOs of Ti whose contribution is contained in figure 3(b). The band OPs of the four systems are given in figures 4(a)–(d) in the same sequence as that of figures 3(a)–(d), where the e/a ratios of the four systems are 4, 4, ∼4.23, and ∼4.46, showing a tendency to increase in this sequence. In each figure, the bonding OP having positive values is indicated by the solid curve presenting the large values below E_f, also given by the horizontal lines, while the anti-bonding OP having the negative values is indicated by the broken curve where the values become significant above E_f. The figures show that the solid curve tends to shift downwards away from E_f as the e/a ratio is increased. Shapes of the solid curves are all similar to each other and commonly reveal the remarkable peak right below E_f, which enables us to measure the electronic band occupation as a depth of the peak denoted by δ in the figures. δ was plotted with respect to e/a. The variation is given in figure 5, where the two points at $e/a = 4$ are the data of both pure and Zr–Ti systems; they are close to
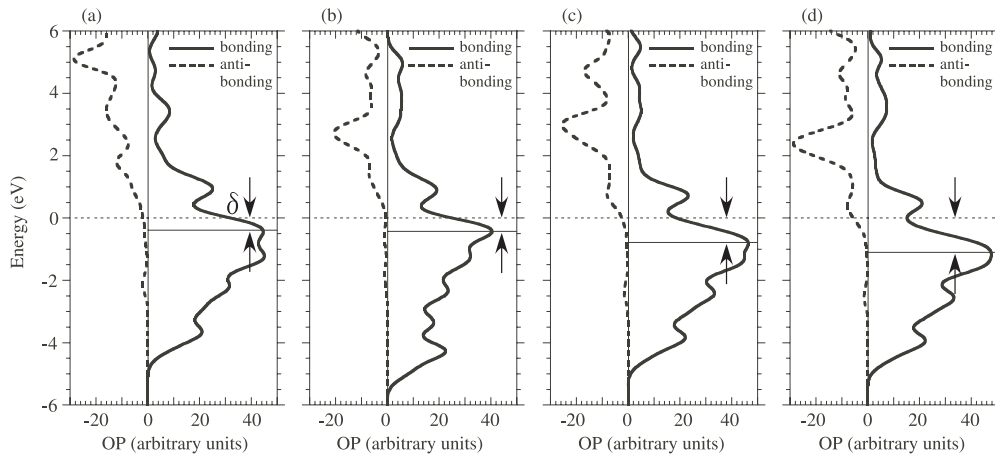
Figure 4. OP diagrams of the four Zr systems. The figures (a)–(d) correspond to figures 3(a)–(d), respectively. Each OP was given by summing the atomic-pair components in the cluster. Each figure shows the remarkable peak of the bonding OP right below E_f. The depth δ is indicated by arrows.
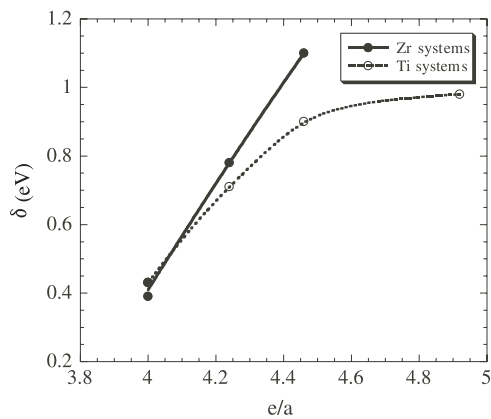
**Figure 5.** δ versus e/a for the Zr and Ti systems.

each other, but the one for the pure system is located slightly below the other one. As shown in the figure, δ is clearly increased with increasing e/a, which means a stabilizing of the structure, and gives no substantial difference in the values between the pure and Zr–Ti systems. This feature suggests that the structure of the latter system is the most unstable among the alloys, which is consistent with our expectation.

Correspondingly, the DOSs and OPs for the pure Ti, Ti–V, Ti–Cr, and Ti–Fe systems are shown in figures 6(a)–(d) and 7(a)–(d), where E_f is also given by the horizontal lines. The e/a is also increased in the sequence (a) through (d), and the values are 4, ∼4.23, ∼4.46, and ∼4.92, respectively. The total DOSs for all systems also present the band near E_f, and the partial DOSs also indicate that the band consists of the 3d AOs of the elements in each system. The bonding and anti-bonding OPs given by the solid and broken curves show the same features as those of the Zr systems, indicating that δ is also increased with increasing e/a as plotted in figure 5. The results imply that electronic stabilization of the structure also occurs in the Ti systems as expected.

In performing the cluster calculation, there might be the following three problems of modeling, suggesting a possibility

of model dependence of the results: (1) the concentration which is universal among the models, (2) the artificial hexagon in the model formed by the solute atoms despite no ordering or clustering being observed [24], and (3) the values of the lattice parameters fixed for all models. To inspect the possibility, a preliminary calculation was done on some of the systems giving variation of the model size, the concentration, and the atomic arrangements so as to maintain the fundamental symmetry. The preliminary results essentially show no qualitative difference from those obtained by the model with the 26 sites described above. Therefore, this employed simple model would supply sufficient quality data for the analysis of the bonding nature. As for the calculation performed by considering the problem (2), we clearly present evidence of 'no essential difference' which was obtained based upon the disordered cluster models of both Zr and Ti alloys.

Figure 8 shows the employed cluster model, where the open and solid circles indicate locations of the solvents and solutes. No change in the frame symmetry, the concentration, or the dimension from those of the model in figure 2 is applied, but the atomic arrangements are quite disordered so that only point symmetry 1 is involved. Figures 9(a)–(c) are the obtained OP diagrams of the Zr systems, and they correspond to those based upon the ordered model, figures 4(b)–(d), respectively. The OP curves in figure 9 also exhibit a peak right below E_f, and show the downward shift of the positive OP component with respect to E_f as e/a is increased. This tendency is quite similar to that of figures 4, meaning that the structure is also stabilized even in the disordered systems. Figures 10(a)–(c) are the diagrams of the Ti systems, corresponding to figures 7(b)–(d). Figure 10 indicate the same tendency as figures 9, also implying the stabilization. The δ values are measured in the same way as the ones for the ordered systems, and the readings of the Zr and Ti systems were plotted versus e/a, as given in figure 11. The two points of both pure systems at $e/a = 4$ are supplied from figure 5; the point of the Zr cluster given by a solid circle is located below the curve, and the other point given by an open circle guides the full curve of the Ti systems. The two curves in figure 11 are similar to
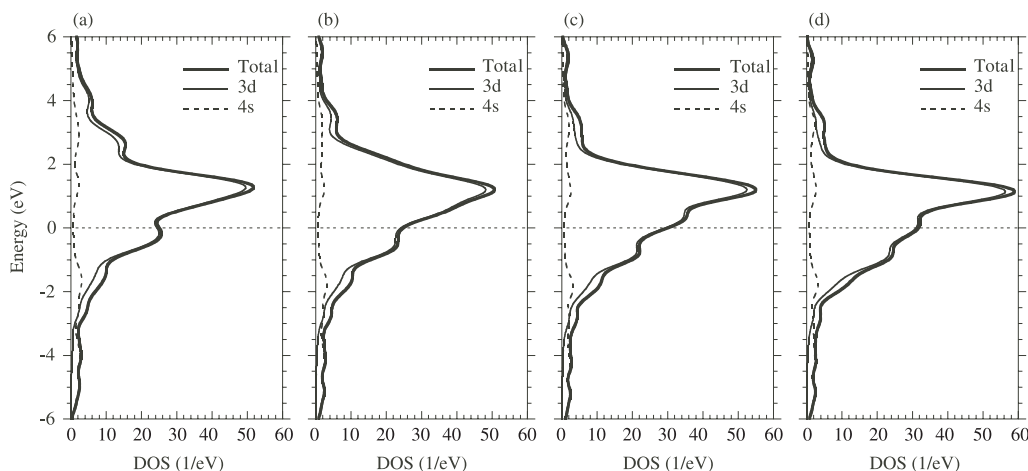
Figure 6. Total and partial DOS curves near the Fermi level for (a) the pure Ti, (b) Ti–V, (c) Ti–Cr, and (d) Ti–Fe systems. Each partial DOS for the alloy was given in the same way as that for figure 3.
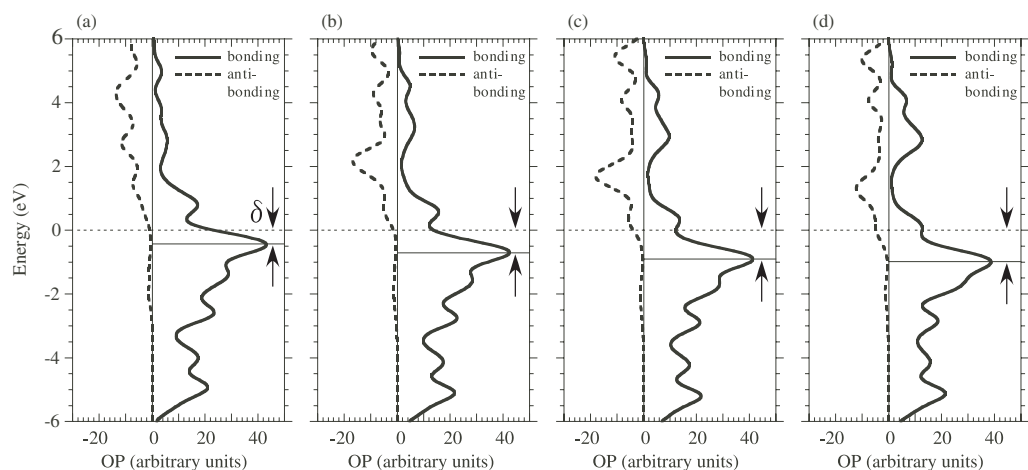
Figure 7. OP diagrams of the four Ti systems. The figures (a)–(d) correspond to figures 6(a)–(d), respectively. Each OP was given in the same way as that for figure 4. Each figure also shows the peak and δ.
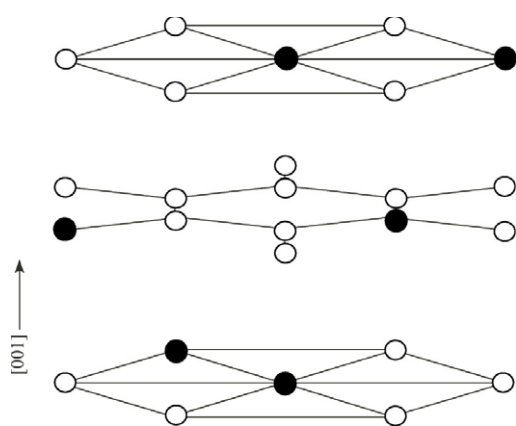

Figure 8. A cluster model made by disordering the atomic arrangements given in figure 2. No point symmetry except 1 is found.

those in figure 5, which allows us to see the electronic effect by using only the typical results obtained from the ordered model.

In addition, comparison of figures 5 and 11 also indicates a difference. Portions of both curves for $e/a > 4$ in figure 11 lie below those in figure 5, while this trend is reversed for both Zr–Ti systems, which suggests a crossover effect of the electronic excess and the chemical order on the phase stability. We leave any discussion of this suggestion out of the current work, since results of the calculation show the electronic stabilization for both ordered and disordered systems, and do not require further investigation here.

The BCC $(1\bar{1}0)$ electron diffraction patterns were observed for the Zr–30, −35, −50 at.% Ti alloys at room temperature, which reproduced characteristics of the intensity distribution obtained in the previous study given in [17]. The distribution of Zr–50 at.% Ti is the most diffuse among the three patterns, leading us to suggest that the system would exhibit the significant temperature dependence through any freezing if it occurred. Figures 12(a) and (b) are the patterns of Zr–50 at.% Ti taken at 295 and 102 K, respectively, with the beam position almost fixed in the single foil. Both patterns show diffuse streaks which are parallel to the $\langle 112 \rangle$ directions or perpendicular to the $\langle 111 \rangle$ directions, giving almost no
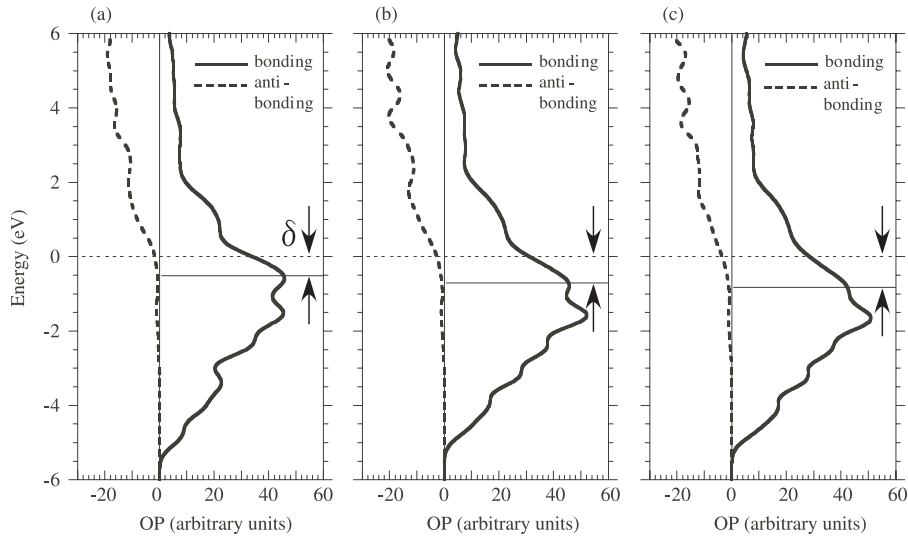
Figure 9. OP diagrams of the disordered Zr systems corresponding to figures 4(b)–(d).
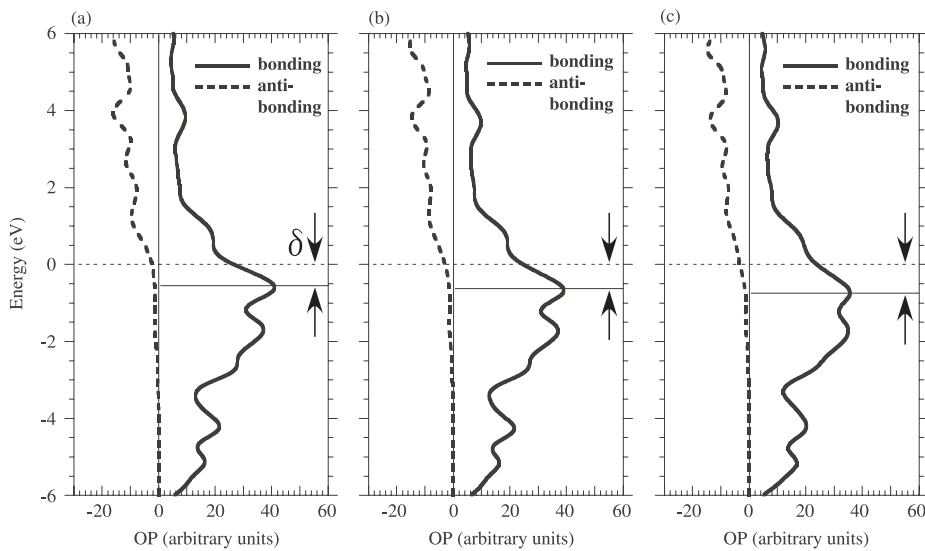

Figure 10. OP diagrams of the disordered Ti systems corresponding to figures 7(b)–(d).

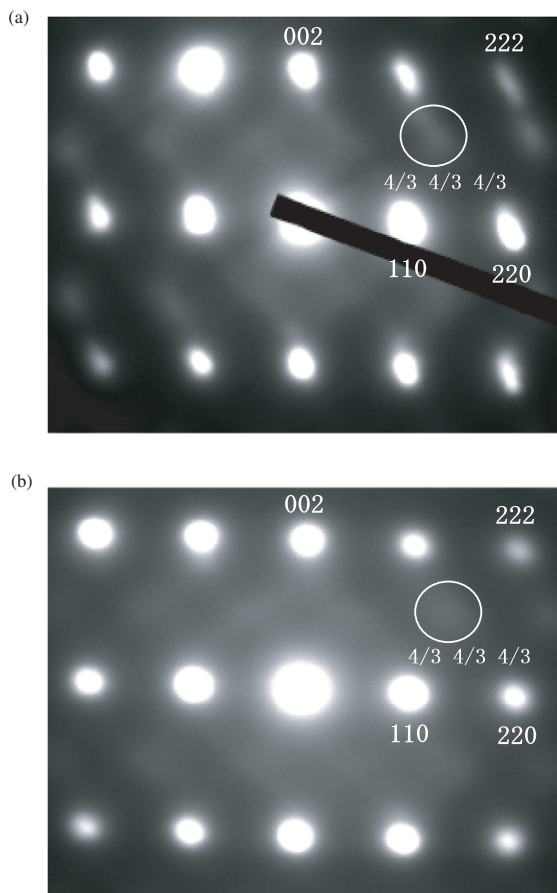appreciable temperature dependence of the distribution. This also agrees with our expectation.

Figures 13(a) and (b) are the reference $(1\bar{1}0)$ patterns taken from Ti–24 mass% V at 295 K and 106 K, respectively. The figure (a) also shows the diffuse streaks whose shapes are slightly circular compared with those in figure 12(a). This distribution feature was originally observed by De Fontain *et al* on Ti–Mo and Ti–Fe alloys [18], and they suggested that the feature implies deformation of phonon dispersion surface caused by the mode–mode coupling. Therefore, the difference of the shapes from those observed in the Zr–50 at.% Ti alloy can be attributed to the anharmonicity of the valence-electronic origin, if the structure is dynamic. Though, a question of which causes the circular distribution, the phonons or the structural fluctuations, remains undetermined, and how this type of coupling physically provides the omega-like elastic fields calculated by De Fontain *et al* [18] is unknown at the

present time. To solve the question, measurements of the neutron inelastic line shapes around the circular distribution are required, if the origin is related to the phonons. Results from a subtle analysis of decoupling the states based upon the anharmonic-lattice potential will provide the characteristic *q*-dependent amplitudes of the eigenmodes. On the other hand, if of static origin, the local structure analysis using the diffuse scattering data must be adequate. The results are supposed to provide the characteristic short-range correlations which may enable us to obtain a key to understand the physical origin of the coupling.

Figure 13(b) indicates the significant variation of the intensity distribution with decreasing temperature. The broad superlattice spots are clearly seen, and the intensities of the streaks are increased, suggesting freezing of the omega phase. The results successfully reproduced those previously obtained by x-ray diffraction [20], and are quite in contrast to the
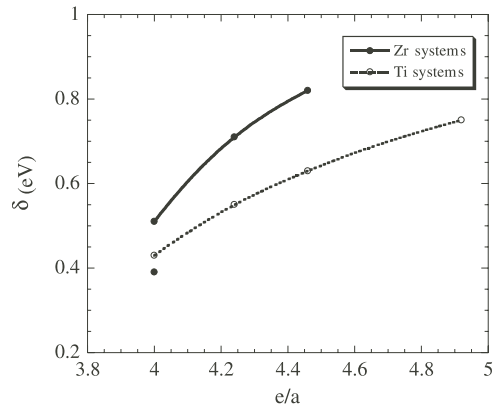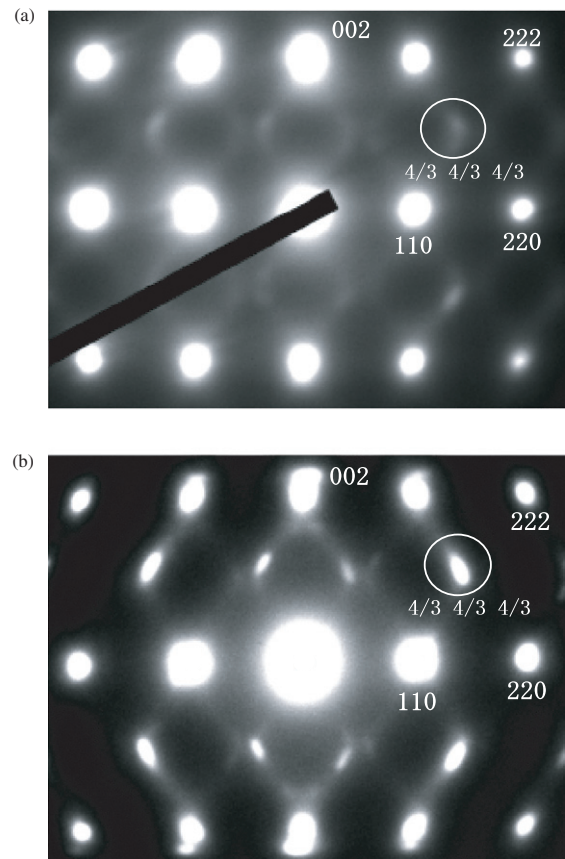
Figure 11. δ versus e/a for the disordered Zr and Ti systems corresponding to figure 5. The plots of the pure Zr and Ti systems were provided from figure 5.

Figure 12. The $(1\bar{1}0)$ electron diffraction patterns obtained from the Zr–50 at.% Ti alloy at (a) 295 K and (b) 102 K. The diffuse scattering around the (4/3, 4/3, 4/3) reciprocal lattice point is singled out by a circle.


Figure 13. The $(1\bar{1}0)$ electron diffraction patterns obtained from the Ti–24 mass% V alloy at (a) 295 K and (b) 106 K. The diffuse scattering is also marked.

temperature dependence observed in the Zr–Ti alloys, which also supports the idea of the valence-electronic effects.

Figure 14(a) shows results of the x-ray diffraction experiment obtained from the Zr–30 at.% Ti system. The two plots indicate the intensity distribution of the (4/3, 4/3, 4/3) superlattice reflection along the [111] direction at 300 K and

30 K, respectively. Each shape exhibits a nearly symmetric single peak (if the background is subtracted), despite the beam consisting of the Kα_1 and Kα_2 rays whose intensity ratio is about 2:1, suggesting that the two broad peaks are closely located so that the two lines are unresolved [20]. Comparison of the two profiles indicates only a slight reduction of the peak intensity but no appreciable broadening or shift of the peak position. This tendency is quite similar to that observed by the electron diffraction.

Figure 14(b) correspondingly provides the reference data which were previously taken from the Ti–24 mass% V alloy at the two temperatures [20]. The 2θ values of the two peaks are slightly larger than those of the Zr alloy since the lattice parameter of the Ti alloy is in fact $\sim$6% smaller. The figure presents a significant temperature dependence also in contrast to that observed in the Zr–Ti alloy. The result is also consistent with that of the electron diffraction.

Figures 15(a)–(f) summarize the temperature dependence of the x-ray intensity distribution of the (4/3, 4/3, 4/3) reflection along the [111] direction. Figures (a)–(c) were drawn using the data obtained from the Zr alloys. The data were taken at temperatures from 30 to 300 K. Each figure shows the relative values of the integrated intensity, the incommensurability, the distribution widths, written as I/I_{30}, $\Delta - \Delta_{30}$, w/w_{30}, and contains a set of three plots given by the data of the Zr–30, -35, -50 at.% Ti alloys, where
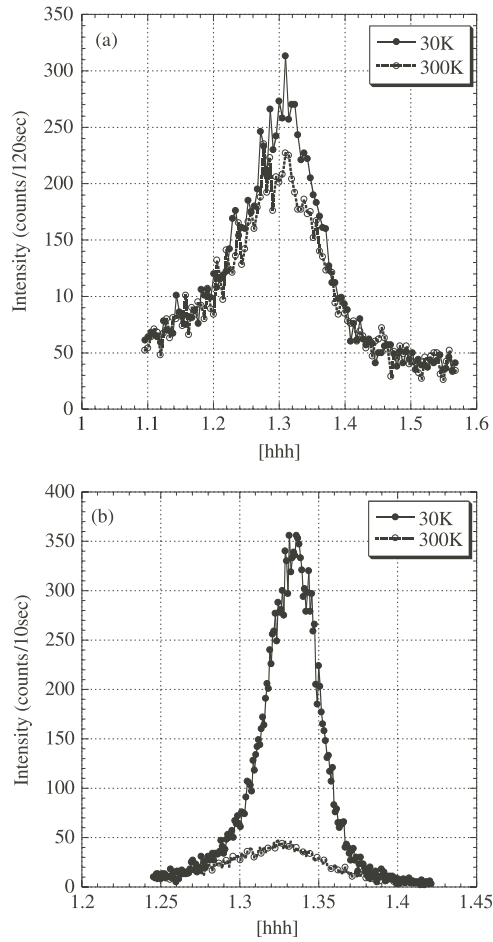
Figure 14. The intensity distribution of the (4/3, 4/3, 4/3) superlattice reflection along the [111] direction obtained from (a) the Zr–30 at.% Ti alloy and (b) the Ti–24 mass% V alloy. Each figure contains the data taken at 300 and 30 K.

I, Δ, w are the data at each temperature, and the three symbols with subscript 30 mean those obtained at 30 K. To determine the values of I, Δ, w, the [111] scan profiles at all temperatures were analyzed using the best-fit single Gaussian, which is the same method as that employed previously [20]. According to this analysis, values of the distribution centers are possibly slightly increased from the real values, and the widths w also increased, because of the intrinsic split of the $K\alpha_1$ and $K\alpha_2$ lines [20]. The changes were defined as the errors, and were previously estimated for the case of the Ti–V alloys [20]. The results are listed in table 1 in [20], where both errors are written as Δq and Δw, respectively. The table tells us that the values of Δq for the (4/3, 4/3, 4/3) reflection are small compared with $|q|$, 0.0025–0.0027 rlu (see columns for the reflection in the table), and Δq itself exhibits relatively tiny change with respect to temperature and concentration; since Δq caused Δw, the constancy is involved in Δw. Therefore, the estimation enables us to expect that Δq is nearly universal for all systems, which gives no problem in determining $\Delta - \Delta_{30}$. On the other hand, Δw in the table decreases significantly with increasing w. Since w, seen in figure 14(a) for both temperature, is typical among the Zr systems and apparently larger than that in figure 14(b),

Δw is expected to be quite trivial, giving no trouble for obtaining w/w_{30}. The three figures basically show tendencies of destabilizing atomic correlations of the omega phase with increasing temperature.

The reference figures to figures 15(a)–(c) are correspondingly given as figures 15(d)–(f). Figures (d)–(f) were produced from the data taken from Ti–20, −24, −27 mass% V alloys in the previous study [20] which qualitatively showed that phase stability of the omega phase of these Ti systems is lowered in the same sequence. The plots were presented by using the values relative to those obtained at the lowest temperature (30 K for the first two systems, and 20 K for the rest). The temperature dependence of the relative values exhibited in the figures (d)–(f) is similar to that in (a)–(c). Mutually comparing the reference figures indicates that the dependence for the 20 and 27 mass% V alloy is significantly weak compared with that for the 24 mass% V alloy. The weak dependence is likely to appear because of a small possibility of thermal destruction of the stable CDW for the 20% system or evolution of the unstable CDW for the 27% system. The further comparison of the figures (a)–(c) with (d)–(f) clearly shows that the temperature dependence for the Zr systems is much less significant than that for the Ti–24 mass% V alloy, and that similar to the dependence for the other two Ti alloys whose phase stability is almost saturated to temperature variation. The weak dependence, despite no valence-electronic effect for the Zr systems, is expected to be simply caused by the athermal nucleation and growth which takes place in classical thermodynamics, where the energy barrier is exceeded by undercooling (or overheating) as well as the lattice distortion of the mechanical origin. All the results of x-ray diffraction show no inconsistency with those obtained from population analysis or electron diffraction.

Features of the phase behavior with respect to temperature observed in this study must also be indicated by the electrical resistivity. The measurement previously done with respect to temperature using Ti–Mo alloys [19], thought to belong to the CDW systems, show that the resistivity exhibits a single peak or a kind of variation at low temperature, suggesting a notional freezing [20]. Based on this fact along with our current results, it is expected that the behavior of the Zr–Ti systems turns out to be like normal metals and less significant than that of the Ti–Mo systems. This speculation might have been seen, but unfortunately no published data to support it has been found.

5. Conclusion

In this study, first-principles population analysis of the molecular orbitals was performed to investigate the valence-electronic effect on phase stability of the omega phase in Ti and Zr alloys, followed by low-temperature electron and x-ray diffraction experiments for qualitative verification of the calculated results. Results of the calculation indicate that an excess of the valence electrons beyond the $e/a = 4$, expected to form the CDW, increases electronic occupation of the positive overlap populations below E_f, but that the Zr–Ti alloy with zero excess is not the case. This tendency given by calculation was found true, whether the alloys are ordered or disordered. The experimental results show that the structural
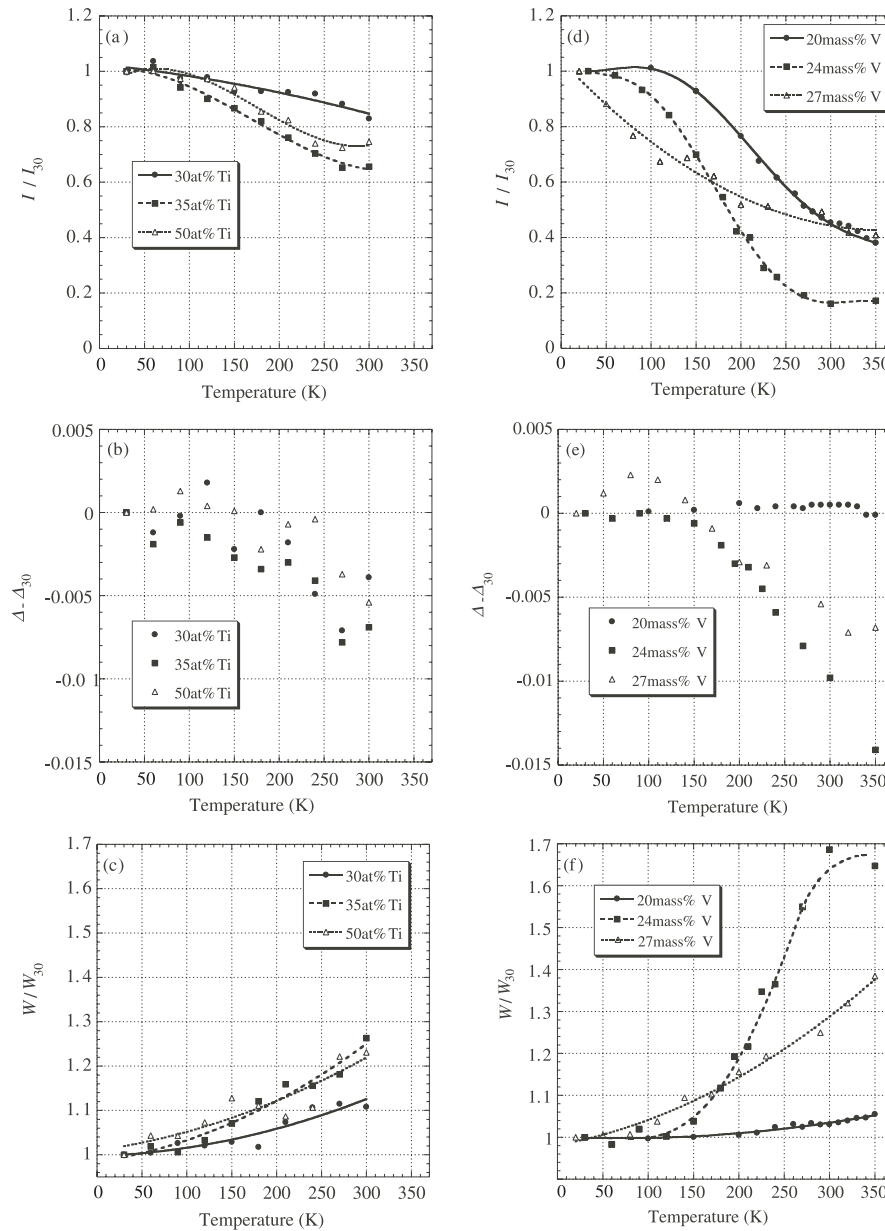
Figure 15. Summary of temperature dependence of the x-ray intensity distribution of the (4/3, 4/3, 4/3) reflection along the [111] direction. The figures (a)–(c) show the dependence of I/I_{30}, $\Delta - \Delta_{30}$, w/w_{30}, obtained from the Zr alloys, respectively. The figures (d)–(f) give the corresponding data for the Ti alloys. Note that the plots for only the 27 mass% V alloy were relative to the data taken at 20 K. The curves in the figures were drawn as guides for the eye. Since the plots in the figure (b) reveal the variation to be quite nonuniform, no guide was applied. The figure (e) is presented in a similar way for comparison.

correlations observed for the prepared samples of the Zr alloys exhibit a small temperature dependence compared with that of the Ti–24 mass% V, which shows the expected electronic effect. Further investigations complementary to this study are being planned.

References

[1] Sass S L 1969 *Acta Metall.* **17** 813
[2] de Fontaine D 1970 *Acta Metall.* **18** 275

[3] Stassis C, Zarestky J and Wakabayashi N 1978 *Phys. Rev. Lett.* **41** 1726

[4] Pynn R 1978 *J. Phys. F: Met. Phys.* **8** 1

[5] Moncton D E, Axe J D and Disalvo F J 1975 *Phys. Rev. Lett.* **34** 734

[6] McMillan W L 1976 *Phys. Rev.* B **14** 1496

[7] Silcock J M, Davies M H and Hardy H K 1955 *Symp. Mechanism of Phase Transformations in Metals (Inst. Metals, London)*

[8] Bagaryatskii Iu A, Nosova G I and Tagunova T V 1955 *Dokl. Akad. Nauk SSSR* **105** 1225

[9] Sass S L and Borie B 1972 *J. Appl. Crystallogr.* **5** 236

[10] Chang A L J, Sass S L and Krakow W 1976 *Acta Metall.* **24** 29

[11] Terauchi H, Sakaue K and Hida M 1981 *J. Phys. Soc. Japan* **50** 3932

[12] Horovitz B, Murray J L and Krumhansl J A 1978 *Phys. Rev.* B **18** 3549

[13] Kuan T S and Sass S L 1976 *Acta Metall.* **24** 1053

[14] Borie B, Sass S L and Andreassen A 1973 *Acta Crystallogr.* A **29** 585

[15] Borie B, Sass S L and Andreassen A 1973 *Acta Crystallogr.* A **29** 594

[16] Borie B and Yakel H L 1983 *Acta Crystallogr.* A **39** 287

[17] Ezaki H, Morinaga M, Kato M and Yukawa N 1991 *Acta Metall.* **39** 1755

[18] de Fontain D, Paton N E and Williams J C 1971 *Acta Metall.* **19** 1153

[19] Sukedai E, Matsumoto H and Hashimoto H 2002 *J. Electron Microsc.* **51** S143

[20] Takesue N 2005 *Phys. Rev.* B **72** 174210

[21] Hatt B A and Williams G I 1959 *Acta Metall.* **7** 682

[22] Slater J C 1974 *Quantum Theory of Molecules and Solids* vol 4 (New York: McGraw-Hill)

[23] Adachi H, Tsukada M and Satoko C 1978 *J. Phys. Soc. Japan* **45** 875

[24] Hida M, Sukedai E and Terauchi H 1988 *Acta Metall.* **36** 1429